DOI:
10.1515/nanoph-2021-0201

Document Version
Peer reviewed version

Optical spin-orbit coupling in the presence of magnetization: photonic skyrmion interaction with magnetic domains

Xinrui Lei[1,2], Luping Du[1,*], Xiaocong Yuan[1,*], Anatoly V. Zayats[2,*]

[1]Nanophotonics Research Centre, Shenzhen Key Laboratory of Micro-Scale Optical Information Technology, Shenzhen University, Shenzhen, Guangdong, 518060, China

[2]Department of Physics and London Centre for Nanotechnology, King's College London, Strand, London, WC2R 2LS, United Kingdom

Abstract: Polarization and related spin properties are important characteristics of electromagnetic waves and their manipulation is crucial in almost all photonic applications. Magnetic materials are often used for controlling light polarization through the magneto-optical Kerr or Faraday effects. Recently, complex topological structures of the optical spin have been demonstrated in the evanescent light field, which in the presence of the spin-orbit coupling may form photonic skyrmions. Here, we investigate the optical spin-orbit coupling in the presence of magnetization and the interaction between photonic skyrmions and magnetic domains. We demonstrate that the magnetization is responsible for the modulation of the optical spin distribution, resulting in twisted Neel-type skyrmions. This effect can be used for the visualization of magnetic domain structure with both in plane and polar orientation of magnetization, and in turn for creation of complex optical spin distributions using magnetization patterns. The demonstrated interplay between photonic skyrmions and magneto-optical effects may also provide novel opportunities for investigation and manipulation of magnetic skyrmions using optical spin-orbit coupling.

Keywords: optical skyrmion, spin-orbit coupling, magneto-optical effects

1. Introduction

Magnetic materials and their nanostructures can influence the polarization state of light upon reflection or transmission due to the Kerr or Faraday effects, respectively, and widely used in photonics for polarization rotators and optical isolators. They are also a cornerstone for data storage applications which are traditionally based on manipulation of magnetic domains. Magnetic skyrmions [1, 2], which are topological nanostructures of magnetization, have attracted recently significant attention for magnetic memory development with low energy requirements. Various magneto optical (MO) techniques are used to study, characterize and visualize the magnetic materials and domains using magnetization-dependent rotation of the polarization plane of light on reflection or transmission from a magnetic sample [3-7]. Such Kerr or Faraday rotation from a ferromagnetic film is weak and require significant macroscopic propagation length to be detected. To enhance the MO activity, metallic nanostructures with plasmonic effects can be employed to increase the effect [8-16].

Prominent optical analogies of magnetic topological structures have been recently demonstrated, such as photonic skyrmions and merons [17-19]. Photonic spin-skyrmions rely on the spin-orbit coupling in the evanescent field of guided modes. Spin angular momentum (SAM), which is related

to circular polarization of light, and orbital angular momentum (OAM) are intrinsic properties of light waves and play a critical role in light–matter interactions [20-23]. This dynamic mutual-conversion between SAM and OAM is enhanced at the nanoscale [24-26] and manifest itself in numerous unusual physical phenomena, such photonic analogue of the quantum spin Hall effect [27, 28], unidirectional coupling to the guided modes [29], chiral detection [30], lateral optical forces [31] as well as topological insulators [32], many of which rely on the transverse spin carrying by the evanescent field of waveguiding modes [33-35]. Spin-orbit coupling provides a new, unexplored degree of freedom for engineering magneto-optical interactions with complex topological structures of light polarization, such as photonic skyrmions.

In this article, we study optical spin-orbit interactions in the presence of magnetization and magneto-optical interactions of photonic skyrmions. We analyze the near-field response of their MO activity for different magnetization orientation. By examining the electromagnetic field in a magneto-plasmonic system, we demonstrate that the photonic skyrmion, which is formed by the spin–orbit coupling in evanescent vortex beam, is modulated in the presence of the MO response as the orientation of magnetization changes. This provides an opportunity for the visualization of magnetic domain structure by observing the spin states of the skyrmion. The superposed spin states of a pair of opposite photonic skyrmions, generated by opposite optical vortices, yield distinct domain contrast with a resolution below 120 nm. Furthermore, due to the different response of photonic skyrmions with opposite topological charges to each magnetization orientation, the spin-based domain observation eliminates the magnetization orientation constrains of conventional Kerr microscopy. The results provide new understanding of optical spin and magnetization interactions and offer novel opportunities for study and manipulation of magnetic structures, including magnetic skyrmions, using optical spin-orbit coupling.

2. Results and discussion

2.1 Magneto-optical interactions in the near-field.

Spin-skyrmions are formed due to spin-orbit coupling in the evanescent field of a guided wave, such as surface plasmon polaritons (SPPs) [17]. Therefore, we consider a general multilayered structure comprising a waveguiding (generally nonmagnetic) layer adjacent to a magnetic film or waveguiding in a magnetic layer itself (Figure 1A). The proposed framework describes the properties of such a multilayer for any position of the magnetic film in the multilayered stack and any illumination direction. The permittivity tensor of a magnetic layer is given by

$$\hat{\varepsilon}_i = \begin{pmatrix} \varepsilon_i & -ig_z & ig_y \\ ig_z & \varepsilon_i & -ig_x \\ -ig_y & ig_x & \varepsilon_i \end{pmatrix}, \tag{1}$$

where ε_i is the relative permittivity of the magnetic material and the off-diagonal elements $g_{x,y,z}$ are gyration vector constants, which are linear in magnetization. By applying the Maxwell's equations, the wave equation inside a magnetic layer takes the form

$$\nabla(\nabla \cdot \mathbf{E}) - \nabla^2 \mathbf{E} = k_0^2 \hat{\varepsilon}_i \mathbf{E}, \tag{2}$$

where k_0 is the wave vector in vacuum. For a surface wave propagating along x axis, the electric field is characterized by $\mathbf{E} = \mathbf{E}_0 e^{i\beta x \pm k_z z}$, with β denoting the propagation constant and the

longitudinal wave vector k_z can be obtained from the nontrivial solutions of electric field $\mathbf{E_0}$ in Equation 2, which depends on the magnetization orientation.

Transversal magnetization (g_x= g_z=0) couples the x and z components of the electric field, maintaining the independence of TE and TM polarized guided modes. From Equation 2, the wavevector inside the magnetic layer takes the relation $k_{zi} = \sqrt{\beta^2 - \varepsilon_i k_0^2}$ for a TE mode or $k_{zi} = \sqrt{\beta^2 - \varepsilon_i k_0^2 (1 - g_y^2 / \varepsilon_i^2)}$ for a TM mode. For a TE polarized surface guided mode, the mode dispersion equation and propagation constant β are the same as for a nonmagnetic or demagnetized system (no off-diagonal components present in Equation 1). While for a TM polarized surface mode, the coupling between E_x and E_z results in a modulation on the propagation constant β, which scales linearly with the gyration vector constant [10, 36, 37].

For polar (g_x= g_y=0) or longitudinal (g_y= g_z=0) magnetization, the separation between TE and TM polarization is not possible because of the coupling of magnetization to E_y. The longitudinal wave vector inside the magnetic layer can be represented as $k_{zi}^{\pm} = k_{zi}^0 \pm \Delta k(g)$, where $k_{zi}^0 = \sqrt{\beta^2 - \varepsilon_i k_0^2}$ and $\Delta k(g)$ is the magneto-optical contribution (See Supplementary Note 1). This birefringence inside the magnetic layer implies a 4×4 transfer matrix to maintain the boundary conditions at each interface, which has been developed in many formalisms to deal with the propagation and reflection problems in stratified anisotropic media [38-42]. Taking into account the smallness of g, the propagation constant β of a surface wave in a multilayer structure (Figure 1A) is practically not influenced by magnetization, while the electric field ratio between the in plane TE and TM components, $\eta = E_y / E_x$, in the upper medium is approximately proportional to g (See Supplementary Note 1).

The near-field MO effect is prominent in the SPP modes supported by a structure containing ferromagnetic layers with the large gyration despite the high Ohmic losses. In view of this, we consider in the following the SPPs at an interface between dielectric (medium 1) and ferromagnetic plasmonic metal (medium 2). For polar magnetization (magnetic field is in z direction, normal to the interface), η can be obtained as

$$\eta_z \approx -\frac{i\varepsilon_1^2 k_0^2}{2(\varepsilon_1 - \varepsilon_2)\varepsilon_2 k_{z1}^2} g_z, \tag{3a}$$

where $k_{z1} = \sqrt{\beta^2 - \varepsilon_1 k_0^2}$, and ε_1 and ε_2 are the relative permittivities of a dielectric and a ferromagnetic metal, respectively (See Supplementary Note 1). While for longitudinal magnetization (magnetic field is in x direction, along the interface and parallel to the SPP propagation direction), the ratio

$$\eta_x \approx \frac{\varepsilon_1^2 k_0^2}{2(\varepsilon_1 - \varepsilon_2)\varepsilon_2 k_{z1}^2} \frac{\beta}{k_{z2}^0} g_x, \tag{3b}$$

where $k_{z2}^0 = \sqrt{\beta^2 - \varepsilon_2 k_0^2}$. For a fixed gyration vector constant g, the ratio of η for the two types of magnetization configurations satisfies $\eta_x / \eta_z = i\beta / k_{z2}^0 = E_z / E_x$, which is attributed to the fact that for a polar magnetization, static magnetic field couples to E_x and E_y, while for longitudinal

magnetization to E_z and E_y with the same coupling constant. For plasmonic ferromagnetic metal [Re(ε_2) << −1], η for the longitudinal magnetization is much smaller than that for the polar configuration.

Simulated transverse electric fields at the air/Co interface under the excitation at a wavelength of 633 nm (Figures 1B and C) confirm prediction of Equation 3, showing the coupling to the TE-polarized electric field component E_y with magnitude depending on the magnetization orientation. Noting that in the absence of magnetization in Co, simulated E_y is zero and E_x is the same as in Figure 1B (See Supplementary Note 2 for details of the simulations).

2.2 Photonic skyrmions in the presence of magnetization.

The spin–orbit interaction in a guided TM or TE polarized electromagnetic field can be introduced by considering an evanescent optical vortex (eOV) in a source free, homogeneous and isotropic medium, which can be described by a Hertz vector potential with a helical phase term in the cylindrical coordinates (r, φ, z) as [45]

$$\Psi = AJ_l(k_r r)e^{il\varphi}e^{-k_z z}, \tag{4}$$

where A is a constant, k_r and k_z are the transverse and longitudinal wavevector components satisfying $k_r^2 - k_z^2 = k^2$ with k denoting the wave vector, l is an integer corresponding to the topological charge of the eOV, and J_l is the Bessel function of the first kind of order l. For a TM (H_z=0) or TE (E_z=0) polarized eOV, the electric fields can be derived from an electric or magnetic Hertz vector potential as

$$\mathbf{E}_{TM} = \nabla(\nabla\cdot\boldsymbol{\pi}_e) - \mu\varepsilon\frac{\partial^2\boldsymbol{\pi}_e}{\partial t^2} = (-k_z\frac{\partial}{\partial r}, -\frac{k_z}{r}\frac{\partial}{\partial\varphi}, k_r^2)\Psi_e \tag{5a}$$

$$\mathbf{E}_{TE} = -\mu\nabla\times\frac{\partial\boldsymbol{\pi}_m}{\partial t} = i\omega\mu(\frac{1}{r}\frac{\partial}{\partial\varphi}, -\frac{\partial}{\partial r}, 0)\Psi_m, \tag{5b}$$

where ε and μ are the absolute permittivity and permeability of the medium, $\boldsymbol{\pi}_e = \Psi_e e^{-i\omega t}\mathbf{e}_z$ and $\boldsymbol{\pi}_m = \Psi_m e^{-i\omega t}\mathbf{e}_z$ are the electric and magnetic Hertz vector potentials with ω denoting the angular frequency of the wave, and Ψ_e and Ψ_m take the form of Equation 4. The electric field distributions for the TM and TE polarized eOVs with topological charge l=1 are shown in Figures 2A and B respectively. For a TM-polarized evanescent vortex beam, the dominant E_z field forms a doughnut-shaped profile. While for the TE-polarized one, the electric field has maximum in the center.

The resulting spatial distribution of a SAM $\mathbf{S} \propto \mathrm{Im}(\mathbf{E}^*\times\mathbf{E})$ can be described by the topological structure similar to a magnetic skyrmion: optical spin-skyrmion. Corresponding skyrmion number, which is calculated as [46] $Q = (1/4\pi)\iint\mathbf{n}\cdot(\partial_x\mathbf{n}\times\partial_y\mathbf{n})dxdy = \pm 1$ with $\mathbf{n}$=$\mathbf{S}$/|S| denoting the unit spin vector, is determined by the sign of topological charge l. For l > 0, the spin vectors tilt progressive from the 'up' state in the centre to the opposite 'down' state along the radial direction, typical for the Neel-type skyrmions with positive skyrmion number (Figure 2C). Skyrmions with negative skyrmion number can be formed as well for l < 0, with spin down in the centre (Figure 2D). The

appearance of this photonic spin topological structure is due to spin-orbit coupling governed by spin-momentum locking in the evanescent field of a surface plasmon polariton [17, 47].

In the presence of a magneto-optical effect, the separation between TM and TE modes is restrained and a superposition of electric and magnetic Hertz vector potentials is required to unveil the spin–orbit interaction. From the near-field MO effect discussed above, the Hertz potentials are linked through the relation

$$\Psi_m = \eta \frac{k_z}{iZk_0} \Psi_e, \tag{6}$$

where η is the in-plane electric field ratio defined in Equation 3 and $Z = \sqrt{\mu/\varepsilon}$ denotes the wave impendence. The coupling between these Hertz potentials modulates the skyrmions formed by either pure electric or pure magnetic Hertz potential with each SAM component affected, so that the modulated skyrmion is transformed into *twisted* Neel-type skyrmion [48, 49] due to the nonzero azimuthal component of SAM S_φ. (Figures 2C-F). The modulation of the skyrmion contains the information of the magnetization of the layer.

In the case of polar magnetization, η is homogeneous for each polar angle φ along the plane. By substituting Equation 6 into Equation 5, the SAM normal to the interface can be obtained as

$$S_z = 2\,\mathrm{Im}(E_r^* E_\varphi) = \frac{A^2 k_r^2 k_z^2 e^{-2k_z z}}{2}[(1+|\eta_z|^2 + 2\,\mathrm{Im}\,\eta_z)J_{l-1}^2(k_r r) - (1+|\eta_z|^2 - 2\,\mathrm{Im}\,\eta_z)J_{l+1}^2(k_r r)], \tag{7}$$

which shows a weak modulation of the spin texture compared to a non-magnetized photonic skyrmion descried by $S_{z0} = \frac{A^2 k_r^2 k_z^2 e^{-2k_z z}}{2}[J_{l-1}^2(k_r r) - J_{l+1}^2(k_r r)]$. By comparing two skyrmions with opposite skyrmion numbers (l = ±1, Figures 2C and D), the magnetization effect can be described as

$$\Delta S_z = S_{z,1} + S_{z,-1} = 2\,\mathrm{Im}\,\eta_z [J_0^2(k_r r) + J_2^2(k_r r)] A^2 \varepsilon k_r^2 k_z^2 e^{-2k_z z}, \tag{8}$$

where sign is determined by the imaginary part of η, in other words, the orientation of magnetization. This gives rise to an opportunity to characterize the magnetization of the various domain structures.

The spin state modulation can be normalized to the field intensity $I_{xy} = |E_r|^2 + |E_\varphi|^2$ as $\gamma_s = \frac{S_z}{I_{xy}}$ so that

$$\Delta\gamma_s = \gamma_{s,1} + \gamma_{s,-1} \approx \mathrm{Im}\,\eta_z \frac{16 J_0^2(k_r r) J_2^2(k_r r)}{[J_0^2(k_r r) + J_2^2(k_r r)]^2}, \tag{9}$$

which can be measured in experiment. In the polar configuration, the skyrmion number is preserved in the presence of magnetization (see Supplementary Note 3).

In the numerical simulations, a tightly focused (NA=1.49) radially polarized (RP) beam (a wavelength of 633 nm) with a spiral phase of topological charge l = ±1 is used to illuminate a sample consisting of a 50-nm-thick cobalt film sandwiched by a silica substrate and air (Figure 3A) (see Supplementary Note 2 for details of the simulations). This provides a SPP excitation and generation of a photonic skyrmion at an air/cobalt interface. For the magnetization oriented in a positive *z* direction, the spin states of opposite skyrmions generated by the RP beams carrying opposite topological charge are shown in Figures 3B and C. This results in the $\Delta\gamma_s$ distribution with non-negative values (Figure 3D), which coincides well with the theoretical calculations using Equation

9 (inset in Figure 3D). Corresponding superimposed spin state for the magnetization oriented in a negative *z* direction shows the opposite sign (Figure 3E). It is worth noting that $\Delta\gamma_s$ is not attenuated away from the centre of the beam despite the high Ohmic losses in a ferromagnetic metal, since the loss influences only the intensity of the wave but not the spin. As predicted by Equation 9, the sign of $\Delta\gamma_s$ is determined by the orientation of magnetization and can act as an effective indicator for magnetic domain observation.

As an example, we consider the magnetization of a cobalt film consisting of two individual domains of opposite magnetization with the domain wall located at $x = 0$ and $x = -1$ (Figures 3F and G). The magnetic contrast is clearly observable through the sign of $\Delta\gamma_s$. The cross-sectional profiles of $\Delta\gamma_s$ marked on Figures 3F and G with green dashed lines demonstrate a sharp MO contrast with a lateral resolution below 120 nm (light green area in Figure H). It should be noted that the domain contrast will be smeared at the position where $J_0(k_r r)\sim 0$ or $J_2(k_r r)\sim 0$ since, according to Equation 9, $\Delta\gamma_s$ for either positive or negative magnetization (Figures 3D and E) is approaching zero as $J_0(k_r r)$ or $J_2(k_r r)$ is close to zero, resulting in an overlap between a domain wall and zero points of $\Delta\gamma_s$. Nevertheless, the domain wall is still visible in the $\Delta\gamma_s$ maps. Since the resolution depends on the in-plane wave vector of the SPP generated at a Co/air interface, higher resolution can be realized by decreasing the incident wavelength, or adding gap layers between cobalt film and air to increase the SPP wave vector.

For in-plane magnetization (transversal and longitudinal cases are not defined separately here for the cylindrical symmetry of illumination), η is inhomogeneous along the surface plane and depends on the projection of the local in-plane wave vector onto the magnetization direction:

$$\Delta\gamma_s \sim \cos(\varphi - \varphi_0)\,\mathrm{Re}\,\eta_{\mathrm{lon}}\,\frac{[J_0^2(k_r r) - J_2^2(k_r r)]^2}{[J_0^2(k_r r) + J_2^2(k_r r)]^2}\,, \tag{10}$$

where φ_0 is the magnetization orientation with respect to *x*-axis and η_{lon} denotes the electric field ratio calculated for the longitudinal magnetization from Equation 3b. In this case, the resulting spin structure cannot be assigned a skyrmion number in the presence of magnetization. Simulated superposed spin states of a pair of opposite skyrmions generated by plasmonic vortices with topological charges $l = \pm 1$ (γ_s for opposite skyrmions separately are shown in Figure S1) exhibit a strong dependence on the magnetization direction (Equation 10), which is determined by φ_0 (Figures 4A-C). Although the 'central zero line', which is normal to the magnetization direction, in the $\Delta\gamma_s$ distributions is of similar appearance to a domain wall in a polar magnetization case in Figure 3F, its origin is completely different. First of all, from Equation 10, $\Delta\gamma_s$ reaches extreme values as $J_0(k_r r)$ or $J_2(k_r r)$ approaches zero for in-plane magnetization (Figures 4A-C), while for polar magnetization, $\Delta\gamma_s$ is approaching zero as $J_0(k_r r)$ or $J_2(k_r r)\sim 0$. This results in the distinguishable spin state patterns between polar and longitudinal magnetizations (cf Figures 3F and 4A). The modulation of the spin states for in-plane magnetization is much smaller than that in a polar case due to the different ratio η, as discussed in Section 2.1. In addition, a cosine function varies slowly near zero points, making the 'central zero line' for in-plane magnetization much wider in Figure 4A than the sharp domain wall in Figure 3F. As shown in Figures 4D-I, the magnetic domain configuration and magnetization direction is observed in the variation of the spin states. It is worth noting that the sign of the oscillations at the central areas in each of the $\Delta\gamma_s$ map in Figure 4 is due to the TE and TM polarized transmission coefficients of the focused beams in the presence of longitudinal magnetization (See supplementary Note 4 and Figures S2 and S3 for details). The proposed technique can provide 2D domain observation capabilities and, in turn, control of the optical spin patterns in a similar manner

(Figure 5).

3. Conclusion and outlook

We have demonstrated and investigated the optical spin-orbit coupling in the presence of the magnetization, as well as the interaction between photonic skyrmions and magnetic domains. We showed that the spin–orbit coupling in the intrinsic near field magneto-optical activity is responsible for the magnetization-modulated photonic skyrmions, which resizes and twists the spin vectors of skyrmoins, transforming them into twisted Neel-type skyrmions. The superimposed spin vectors of a pair of skyrmions with opposite skyrmion numbers can act as a straightforward and flexible indicator for the magnetization orientation, which gives rise to the visualization of magnetic domain structure. By employing plasmonic vortices formed at the surface of a thin cobalt film, we demonstrated the resolution for the magnetic domain contrast below 120 nm in a case of polar magnetization. Due to different response of photonic skyrmions for each magnetization orientation, same domain observation configuration can be applied for both in plane and out of plane magnetization. The studied magnetization-induced spin-orbit coupling may be important for investigations and applications of novel magneto-optical effects in waveguiding and nanophotonic geometries, as well as manipulation of magnetic skyrmions.

Acknowledgements: This work was supported by the UK Engineering and Physical Sciences Research Council (EP/M013812/1), European Research Council iCOMM project (789340), National Natural Science Foundation of China grants U1701661, 61935013, 62075139, 61427819, 61622504 and 61705135, Guangdong Major Project of Basic Research No. 2020B0301030009, Leadership of Guangdong province program grant 00201505, Natural Science Foundation of Guangdong Province grant 2016A030312010, Science and Technology Innovation Commission of Shenzhen grants RCJC20200714114435063, JCYJ20200109114018750, and Shenzhen Peacock Plan KQTD2015071016560101 and KQTD20170330110444030. L.D. acknowledges the support given by the Guangdong Special Support Program.

Author contribution: All the authors have accepted responsibility for the entire content of this submitted manuscript and approved submission.

Conflict of interest statement: The authors declare no conflicts of interest regarding this article.

References

[1] X. Z. Yu, Y. Onose, N. Kanazawa, et al., "Real-space observation of a two-dimensional skyrmion crystal," Nature **465**, 901-904 (2010).

[2] N. Romming, C. Hanneken, M. Menzel, et al., "Writing and deleting single magnetic skyrmions," Science **341**, 636-639 (2013).

[3] F. Schmidt, and A. Hubert, "Domain observations on CoCr-layers with a digitally enhanced Kerr-microscope," Journal of magnetism and magnetic materials **61**, 307-320 (1986).

[4] W. Dickson, S. Takahashi, R. Pollard, R. Atkinson, and A. V. Zayats, "High-Resolution Optical Imaging of Magnetic-Domain Structures," IEEE Transactions On Nanotechnology **4**, 229-237 (2005).

[5] R. Schäfer, "Investigation of Domains and Dynamics of Domain Walls by the Magneto-optical K err-effect," Handbook of magnetism and advanced magnetic materials (2007).
[6] J. McCord, "Progress in magnetic domain observation by advanced magneto-optical microscopy," Journal of Physics D: Applied Physics **48**, 333001 (2015).
[7] A. Hubert, and R. Schäfer, *Magnetic domains: the analysis of magnetic microstructures* (Springer Science & Business Media, 2008).
[8] C. Hermann, V. Kosobukin, G. Lampel, J. Peretti, V. Safarov, and P. Bertrand, "Surface-enhanced magneto-optics in metallic multilayer films," Physical Review B **64** (2001).
[9] A. Christ, S. G. Tikhodeev, N. A. Gippius, J. Kuhl, and H. Giessen, "Waveguide-plasmon polaritons: strong coupling of photonic and electronic resonances in a metallic photonic crystal slab," Phys Rev Lett **91**, 183901 (2003).
[10] J. B. González-Díaz, A. García-Martín, G. Armelles, et al., "Surface-magnetoplasmon nonreciprocity effects in noble-metal/ferromagnetic heterostructures," Physical Review B **76** (2007).
[11] B. Fan, M. E. Nasir, L. H. Nicholls, A. V. Zayats, and V. A. Podolskiy, "Magneto-Optical Metamaterials: Nonreciprocal Transmission and Faraday Effect Enhancement," Advanced Optical Materials **7**, 1801420 (2019).
[12] B. Sepulveda, J. B. Gonzalez-Diaz, A. Garcia-Martin, L. M. Lechuga, and G. Armelles, "Plasmon-induced magneto-optical activity in nanosized gold disks," Phys Rev Lett **104**, 147401 (2010).
[13] V. I. Belotelov, I. A. Akimov, M. Pohl, et al., "Enhanced magneto-optical effects in magnetoplasmonic crystals," Nat Nanotechnol **6**, 370-376 (2011).
[14] G. Armelles, A. Cebollada, A. García-Martín, and M. U. González, "Magnetoplasmonics: Combining Magnetic and Plasmonic Functionalities," Advanced Optical Materials **1**, 10-35 (2013).
[15] L. E. Kreilkamp, V. I. Belotelov, J. Y. Chin, et al., "Waveguide-Plasmon Polaritons Enhance Transverse Magneto-Optical Kerr Effect," Physical Review X **3** (2013).
[16] N. Maccaferri, X. Inchausti, A. García-Martín, et al., "Resonant Enhancement of Magneto-Optical Activity Induced by Surface Plasmon Polariton Modes Coupling in 2D Magnetoplasmonic Crystals," ACS Photonics **2**, 1769-1779 (2015).
[17] L. Du, A. Yang, A. V. Zayats, and X. Yuan, "Deep-subwavelength features of photonic skyrmions in a confined electromagnetic field with orbital angular momentum," Nature Physics **15**, 650-654 (2019).
[18] S. Tsesses, E. Ostrovsky, K. Cohen, B. Gjonaj, N. H. Lindner, and G. Bartal, "Optical skyrmion lattice in evanescent electromagnetic fields," Science **361**, 993-996 (2018).
[19] X. Lei, A. Yang, P. Shi, et al., "Photonic spin lattices: symmetry constraints for skyrmion and meron topologies," arXiv preprint arXiv:2103.15366 (2021).
[20] L. Allen, S. M. Barnett, and M. J. Padgett, *Optical angular momentum* (CRC press, 2003).
[21] A. T. O'Neil, I. MacVicar, L. Allen, and M. J. Padgett, "Intrinsic and extrinsic nature of the orbital angular momentum of a light beam," Phys Rev Lett **88**, 053601 (2002).
[22] S. M. Barnett, "Optical angular-momentum flux," Journal of Optics B: Quantum and Semiclassical Optics **4**, S7 (2001).
[23] A. Bekshaev, K. Y. Bliokh, and M. Soskin, "Internal flows and energy circulation in light beams," Journal of Optics **13**, 053001 (2011).

[24] K. Y. Bliokh, F. J. Rodríguez-Fortuño, F. Nori, and A. V. Zayats, "Spin–orbit interactions of light," Nature Photonics **9**, 796-808 (2015).
[25] J. Petersen, J. Volz, and A. Rauschenbeutel, "Chiral nanophotonic waveguide interface based on spin-orbit interaction of light," Science **346**, 67-71 (2014).
[26] D. O'Connor, P. Ginzburg, F. J. Rodriguez-Fortuno, G. A. Wurtz, and A. V. Zayats, "Spin-orbit coupling in surface plasmon scattering by nanostructures," Nat Commun **5**, 5327 (2014).
[27] K. Y. Bliokh, D. Smirnova, and F. Nori, "Quantum spin Hall effect of light," Science **348**, 1448-1451 (2015).
[28] T. Van Mechelen, and Z. Jacob, "Universal spin-momentum locking of evanescent waves," Optica **3**, 118 (2016).
[29] F. J. Rodriguez-Fortuno, G. Marino, P. Ginzburg, et al., "Near-field interference for the unidirectional excitation of electromagnetic guided modes," Science **340**, 328-330 (2013).
[30] L. Du, S. S. Kou, E. Balaur, et al., "Broadband chirality-coded meta-aperture for photon-spin resolving," Nat Commun **6**, 10051 (2015).
[31] L. Wei, A. V. Zayats, and F. J. Rodriguez-Fortuno, "Interferometric Evanescent Wave Excitation of a Nanoantenna for Ultrasensitive Displacement and Phase Metrology," Phys Rev Lett **121**, 193901 (2018).
[32] M. Z. Hasan, and C. L. Kane, "Colloquium: Topological insulators," Reviews of Modern Physics **82**, 3045-3067 (2010).
[33] K. Y. Bliokh, and F. Nori, "Transverse spin of a surface polariton," Physical Review A **85** (2012).
[34] K. Y. Bliokh, A. Y. Bekshaev, and F. Nori, "Extraordinary momentum and spin in evanescent waves," Nat Commun **5**, 3300 (2014).
[35] A. Aiello, P. Banzer, M. Neugebauer, and G. Leuchs, "From transverse angular momentum to photonic wheels," Nature Photonics **9**, 789-795 (2015).
[36] V. V. Temnov, G. Armelles, U. Woggon, et al., "Active magneto-plasmonics in hybrid metal–ferromagnet structures," Nature Photonics **4**, 107-111 (2010).
[37] D. Martín-Becerra, J. B. González-Díaz, V. V. Temnov, et al., "Enhancement of the magnetic modulation of surface plasmon polaritons in Au/Co/Au films," Applied Physics Letters **97**, 183114 (2010).
[38] D. W. Berreman, "Optics in stratified and anisotropic media: 4× 4-matrix formulation," Josa **62**, 502-510 (1972).
[39] M. Vassell, "Structure of optical guided modes in planar multilayers of optically anisotropic materials," JOSA **64**, 166-173 (1974).
[40] P. Yeh, "Optics of anisotropic layered media: a new 4× 4 matrix algebra," Surface Science **96**, 41-53 (1980).
[41] J. Zak, E. Moog, C. Liu, and S. Bader, "Universal approach to magneto-optics," Journal of Magnetism and Magnetic Materials **89**, 107-123 (1990).
[42] Š. Višňovský, R. Lopušník, M. Bauer, J. Bok, J. Fassbender, and B. Hillebrands, "Magnetooptic ellipsometry in multilayers at arbitrary magnetization," Optics express **9**, 121-135 (2001).
[43] P. Johnson, and R. Christy, "Optical constants of transition metals: Ti, v, cr, mn, fe, co, ni, and pd," Physical review B **9**, 5056 (1974).
[44] A. K. Zvezdin, and V. a. c. A. Kotov, *Modern magnetooptics and magnetooptical materials* (CRC Press, 1997).

[45] A. Ishimaru, *Electromagnetic wave propagation, radiation, and scattering from fundamentals to applications* (Wiley Online Library, 2017).

[46] N. Nagaosa, and Y. Tokura, "Topological properties and dynamics of magnetic skyrmions," Nat Nanotechnol **8**, 899-911 (2013).

[47] P. Shi, L. Du, C. Li, A. V. Zayats, and X. Yuan, "Spin-momentum law for structured guided modes: the generalized quantum spin-Hall effect for light," arXiv preprint arXiv:1910.03904 (2019).

[48] F. N. Rybakov, A. B. Borisov, and A. N. Bogdanov, "Three-dimensional skyrmion states in thin films of cubic helimagnets," Physical Review B **87** (2013).

[49] S. L. Zhang, G. van der Laan, W. W. Wang, A. A. Haghighirad, and T. Hesjedal, "Direct Observation of Twisted Surface skyrmions in Bulk Crystals," Phys Rev Lett **120**, 227202 (2018).

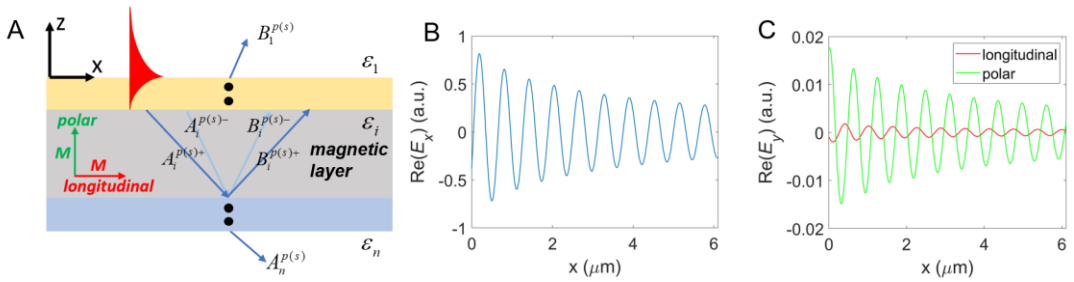

Figure 1: (A) Geometry of surface wave propagation in a multilayer consisting of both magnetic and nonmagnetic layers. Red and green arrows represent the magnetization orientation corresponding to longitudinal and polar magnetization, respectively. (B-C) Simulated in-plane electric fields, propagating in x direction at an interface of air and magnetized semi-infinite medium (Co): (B) E_x and (C) E_y field components for different magnetization orientations. The difference between the E_x fields in the case of polar and longitudinal magnetizations is negligible. The permittivity ε_2 and the gyration vector g of Co are taken from the experimental data as $\varepsilon_2 = -12.5+18.46i$ [43] and $g = 0.59-0.48i$ [44].

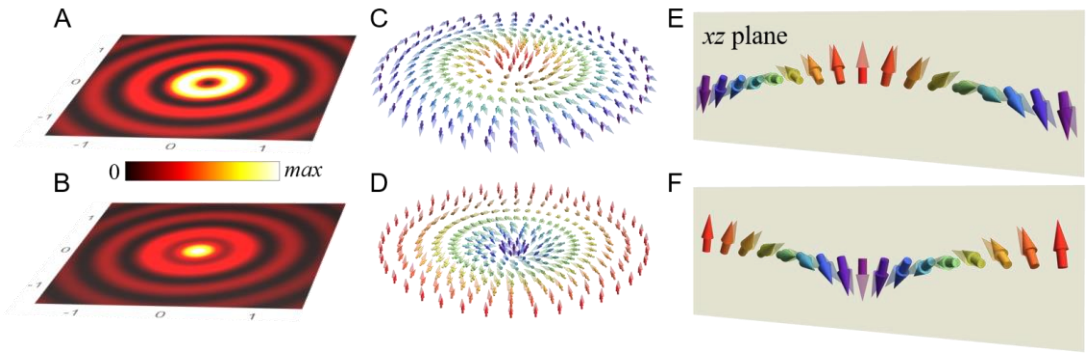

Figure 2: (A,B) Electric field profile of (A) TM polarized evanescent vortex induced by an electric Hertz vector potential and (B) TE polarized evanescent vortex induced by a magnetic Hertz vector potential, both with topological charge $l = 1$ in the absence of magnetization. (C) Distribution of the photonic spin orientations formed by the evanescent vortex beam with topological charge $l = 1$. The opaque arrows indicate the direction of the unit spin vector in (A), while the semitransparent arrows represent the modulated spin vectors in the presence of the polar MO effect. (D) The same as (C) for a topological charge $l = -1$. (E,F) Cross-sections along y=0 plane in (C) and (D) respectively. The in plane wavevector (k_r) of the evanescent vortex for the simulations is set to $1.012k$, where k is the wavevector in the medium, and η is set to 0.3+0.03i.

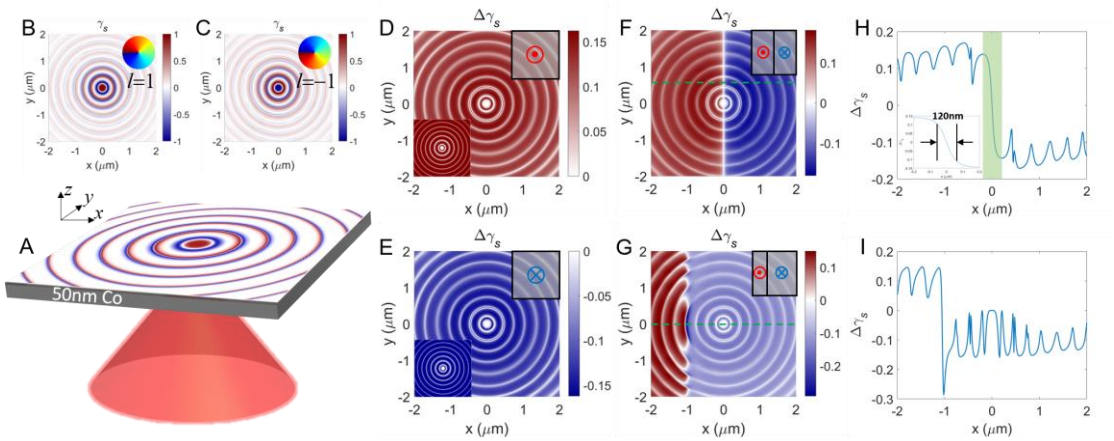

Figure 3: (A) Schematic diagram for the generation of a photonic skyrmion in a ferromagnetic material on the example of the SPP excited on a surface of a thin (50 nm) Co film by a tightly focused (NA=1.49) radially polarized beam. Incident angles below 40° are blocked to stabilize the generation of photonic skyrmions. The permittivity and the gyration vector constant of cobalt at wavelength of 633 nm are the same as in Figure 1. (B-C) Spin states of (B) positive and (C) negative skyrmions generated with $l = \pm 1$ RP beam, respectively, with the Co magnetization in positive z direction. (D) Spatial distribution of $\Delta\gamma_s$ for the skyrmions in (B) and (C). Corresponding theoretical $\Delta\gamma_s$ obtained from Equation 9 is depicted in the bottom left inset. (E) The same as (D) for the magnetization oriented in negative z direction. (F-G) Spatial distribution of $\Delta\gamma_s$ for the magnetic structure consisting of two domains with opposite magnetization orientation: the domain wall is at (F) $x = 0$ and (G) $x = -1\ \mu m$. (H,I) Cross-sections marked in (F,G) with a green dashed line. Inset in (H) is a zoomed view of the spin structure of the area indicated with light green box in (H).

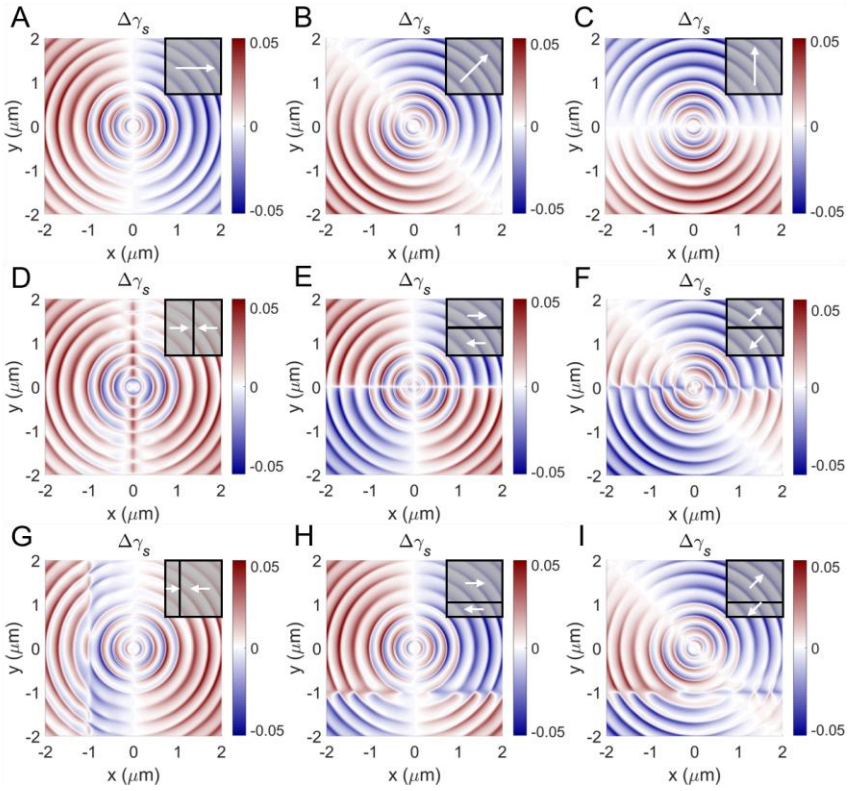

Figure 4: (A-C) Simulated distributions of $\Delta\gamma_s$ for different magnetization orientations in the plane of the film (*xy* plane): (A) $\varphi_0 = 0$, (B) $\varphi_0 = \pi/4$, (C) $\varphi_0 = \pi/2$. (D-I) The same as (A-C) for the domain structure with the domain wall located at (D) $x = 0$, (E-F) $y = 0$, (G) $x = -1$ μm, (H-I) $y = -1$ μm. The magnetic domain can be visualized by the features of $\Delta\gamma_s$ distributions, while the magnetization orientation can be unveiled from the 'central zero line', which is normal to the magnetization direction. Inserts show the magnetization orientation in the domains. The illumination configuration is the same as in Figure 3A.

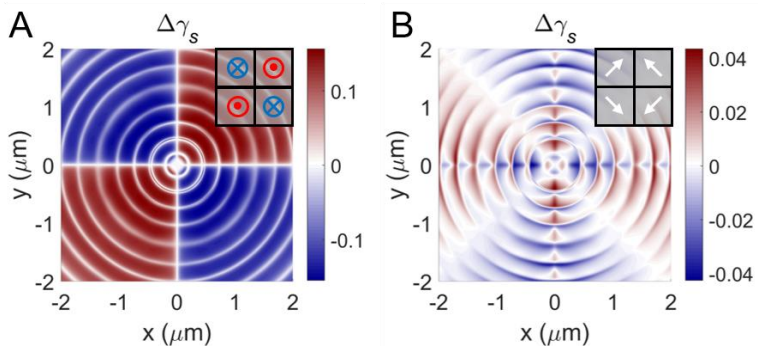

Figure 5: Simulated spatial distributions of $\Delta\gamma_s$ for the domain structures with two orthogonal domain walls located at $x = 0$ and $y = 0$: (A) polar magnetization and (B) in-plane magnetization. Inserts show the magnetization orientation in the domains. The illumination configuration is the same as in Figure 3A.